RAA 2020 Vol. **20** No. **10**, 160(16pp) doi: 10.1088/1674-4527/20/10/160

http://www.raa-journal.org *http://iopscience.iop.org/raa*

Research in Astronomy and Astrophysics

Observational signatures of close binaries of supermassive black holes in active galactic nuclei

Jian-Min Wang[1,2,3] and Yan-Rong Li[1]

[1] Key Laboratory of Particle Astrophysics, Institute of High Energy Physics, Chinese Academy of Sciences, Beijing 100049, China; *wangjm@ihep.ac.cn*
[2] School of Astronomy and Space Science, University of Chinese Academy of Sciences, Beijing 100049, China
[3] National Astronomical Observatories, Chinese Academy of Sciences, Beijing 100101, China

Received 2020 July 29; accepted 2020 August 15

Abstract Inspired by the General Relativity for many decades, experimental physicists and astronomers have a solid dream to detect gravitational waves (GWs) from mergers of black holes, which came true until the excellent performance of the Laser Interferometer Gravitational-Wave Observatory (LIGO) at hundreds Hz. Nano-Hz GWs are expected to be radiated by close-binaries of supermassive black holes (CB-SMBHs; defined as those with separations less than $\sim$0.1 pc) formed during galaxy mergers and detected through the Pulsar Timing Array (PTA) technique. As of the writing, there remains no nano-Hz GWs detection. Searching for CB-SMBHs is also observationally elusive though there exist a number of possible candidates. In this review, we focus on observational signatures of CB-SMBHs from theoretic expectations, simulations and observations. These signatures appear in energy distributions of multiwavelength continuum, long term variations of continuum, jet morphology, reverberation delay maps and spectroastrometry of broad emission lines, AGN type transitions between type-1 and type-2 (changing-look), and gaseous dynamics of circumbinary disks, etc. Unlike hundred-Hz GWs from stellar mass black hole binaries, the waveform chirping of nano-Hz GWs is too slow to detect in a reasonable human timescale. We have to resort to electromagnetic observations to measure orbital parameters of CB-SMBHs to test nano-Hz GW properties. Reverberation mapping is a powerful tool for probing kinematics and geometry of ionized gas in the gravitational well of SMBHs (single or binary) and therefore provides a potential way to determine orbital parameters of CB-SMBHs. In particular, a combination of reverberation mapping with spectroastrometry (realized at the Very Large Telescope Interferometer) will further reinforce this capability. The Atacama Large Millimeter/submillimeter Array (ALMA) and the forthcoming Square Kilometre Array (SKA) are suggested to reveal dynamics of circumbinary disks through molecular emission lines.

Key words: galaxies: active — quasars: supermassive black holes — gravitational waves

1 INTRODUCTION

Active galactic nuclei (AGNs) are generally regarded as celestial objects with supermassive black holes (SMBHs) residing in their nuclei, which accrete medium gas from surrounding environments and serve as the engine for the huge radiation powers of AGNs. Another widely used term "quasar" conventionally refers to those AGNs with the host galaxies not easily distinguished, i.e., extremely luminous AGNs (Rees 1984). The huge radiation power also makes AGNs easy to observe across a wide range of redshift. Nowadays, the observed populations of AGNs and quasars have reached a half million or so from the Sloan Digital Sky Surveys (SDSS; Lyke et al. 2020) and this number will ever increase from the survey of the Dark Energy Spectroscopic Instrument (DESI; Flaugher & Bebek 2014). It is assured that AGNs and quasars are ubiquitous in the Universe.

As expected from the theory of the hierarchical mergers of galaxy evolution, CB-SMBHs evolving from dual galactic cores must be located at centers of some (if not all) galaxies for some times (Begelman et al. 1980; Volonteri et al. 2003; Wang & Ip 2020). Searching for close-binaries of supermassive black holes (CB-SMBHs; defined as those with separations less than $\sim$0.1 pc) has become a hot topic in contemporary astrophysics. Figure 1 shows black hole growth through successive mergers cross cosmic time. At large separations after galaxy mergers,

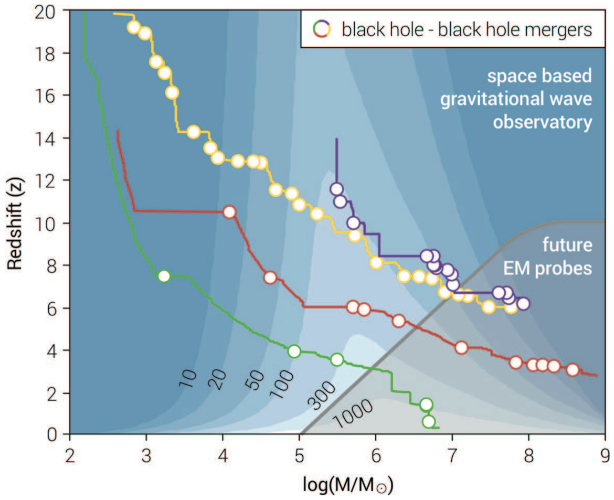

Fig. 1 Black hole growth through mergers of seed black holes cross cosmic time. Black hole binaries are unavoidable phases of galaxy mergers in cosmic evolution. Adapted from eLISA Consortium et al. (2013).

the dynamical friction arising from background stars and matter controls the orbital evolution of each black hole (Milosavljević & Merritt 2001; Yu 2002; Wang & Yuan 2012). At smaller separations ($\sim$ 10pc), three-body interactions between the black hole binaries and stars passing close to the binaries come into effect. However, three-body interaction becomes inefficient when the mass enclosed in the binary orbits are comparable with the total mass of the CB-SMBH in gas-poor environment. As a result, the CB-SMBHs will stall at separations of parsec scales and hardly evolve into the gravitational wave (GW) radiation stage. This is the well-known "final parsec problem" (Begelman et al. 1980; Milosavljević & Merritt 2001). The CB-SMBHs can continue to shrink only when there are some additional mechanisms that are able to efficiently remove the orbital angular momentum (Milosavljević & Merritt 2001). There have been great efforts made to describe the final parsec problem and to solve it with various dynamical processes, such as non-axisymmetric stellar distributions (e.g., Yu 2002; Berczik et al. 2006) and gravitational drags from massive gaseous disks (e.g., Escala et al. 2005; Mayer et al. 2007). However, no consensus has yet been reached on the viable mechanisms.

Although dual AGNs are quite common among galaxies (Comerford et al. 2013; Fu et al. 2015; Liu et al. 2018; Wang et al. 2019) as revealed by the double-peaked features of [O III] line in a large sample of SDSS quasars (Wang et al. 2009; Ge et al. 2012), observational evidence for CB-SMBHs remains elusive (Popović 2012; Dotti et al. 2012). There have been several possible observational signatures used to search for CB-SMBH candidates (see below for details). Notwithstanding, we bear in mind that most phenomena of AGN activities can be explained by accretion onto *single* SMBHs (Rees 1984; Osterbrock & Mathews 1986), implying that most CB-SMBHs probably have finished their final coalescences. This also probably indicates a low occupation of observable CB-SMBHs in galaxies and therefore means big challenges in identifying CB-SMBH candidates. By far the most compact candidate yet found directly from high-spatial resolution radio images is in the interacting galaxy NGC 7674, whose radio map in the nuclei shows two radio cores with a projected separation of 0.35 pc (Kharb et al. 2017). Table 1 summarizes the individually reported candidates of CB-SMBHs via different searching approaches in the literature. There are also a few hundreds of candidates identified from systematic searches over large time-domain surveys (e.g., Graham et al. 2015b; Charisi et al. 2016; Liu et al. 2019).

There already exist many review articles on the formation and observational features of binary supermassive black holes, among which include Begelman et al. (1980), Komossa (2006), Popović (2012), Tanaka & Haiman (2013), Colpi (2014), Roedig & Sesana (2014), De Rosa et al. (2019), etc. Most of the reviews have centered around evolution of black hole pairs from kilo-parsec to parsec scales during galaxy mergers, or around very late stages prior to coalescences. In this review paper, we focus on observational signatures of CB-SMBHs and possible methods to determine their orbital parameters. These CB-SMBHs are radiating GWs, some of which could be strong enough to detect through PTA networks and therefore provide plenty of opportunities for testing nano-Hz GWs.

2 GENERAL PICTURES

Supposing binary black holes with masses of (M_1, M_2) and a separation (a), the orbital period is given by

$$P_{\rm orb} = 2\pi\sqrt{\frac{a^3}{G(M_1+M_2)}} = 3.1\, a_3^{3/2} M_8 (1+q)^{-1/2}\,{\rm yr}, \tag{1}$$

where G is the gravitational constant, $M_8 = M_1/10^8 M_\odot$ is the primary mass, $q = M_2/M_1$ is the mass ratio, $a_3 = a/10^3 R_{\rm g}$ is the orbital separation, and $R_{\rm g} = GM_1/c^2$. Below we introduce the generic evolutionary pathway of CB-SMBHs, cavity formation, and geometric configurations of CB-SMBH systems.

2.1 Evolutionary Pathway of CB-SMBHs

The dynamical evolution of a pair of massive black holes from large separations to final coalescences undergoes several stages (e.g., Begelman et al. 1980; Yu 2002; Merritt 2006).

Table 1 Individually Reported Candidates of CB-SMBHs in the Literature

Name	Redshift	Signatures	Ref.
Akn 120	0.0327	periodic variations	Li et al. (2019)
NGC 1068	0.0038	gas dynamics of nuclei	Wang et al. (2020)
NGC 4151	0.0033	periodic variations	Bon et al. (2012)
NGC 5548	0.0175	periodic variations	Li et al. (2016)
NGC 7674	0.0029	radio image	Kharb et al. (2017)
Mrk 231	0.0422	continuum deficit	Yan et al. (2015)
OJ 287	0.3056	periodic variations	Valtonen et al. (2008)
PG 1302-102	0.2784	periodic variations	Graham et al. (2015b)
SDSS J0159+0105	0.2170	periodic variations	Zheng et al. (2016)
SDSS J1201+3003	0.1460	flux drops in the tidal disruption event	Liu et al. (2014)

(1) Dynamical friction stage: after a galaxy merger event, each black hole embedded in the progenitor galaxy independently sinks toward the center of the newly forming galaxy due to dynamical friction of dark matter, stars as well as interstellar gas. This occurs on the Chandrasekhar dynamical friction time-scale,

$$t_{\rm df} \sim \frac{4\times 10^6}{\log N}\left(\frac{\sigma_c}{200{\rm km\ s^{-1}}}\right)\left(\frac{r_c}{100{\rm pc}}\right)^2 M_8^{-1}{\rm yr}, \quad (2)$$

where the galaxy core is presumed to have a velocity dispersion σ_c, a core radius r_c and contain N stars.

(2) Non-hard binary stage: when the black hole separation falls below the gravitational influence radius

$$\begin{aligned} a &\lesssim \frac{G(M_1+M_2)}{\sigma_c^2} \\ &\approx 10\left(\frac{M_1+M_2}{10^8 M_\odot}\right)\left(\frac{\sigma_c}{200{\rm km\ s^{-1}}}\right)^{-2}{\rm pc}, \end{aligned} \quad (3)$$

the two black holes form a gravitationally bound binary system. The system then experiences a rapid orbital decay driven by the combined effects of dynamical friction and three-body interactions between the black hole binary and stars passing into its vicinity.

(3) Hard binary stage: when the specific binding energy of the binary exceeds the typical specific binding energy of stars, the binary system comes to the hard binary phase,

$$\begin{aligned} a &\lesssim a_{\rm h} = \frac{G\mu}{4\sigma_c^2} \\ &= 2.5\frac{q}{(1+q)^2}\left(\frac{M_1+M_2}{10^8 M_\odot}\right)\left(\frac{\sigma_c}{200{\rm km\ s^{-1}}}\right)^{-2}{\rm pc}, \end{aligned} \quad (4)$$

where $\mu = M_1M_2/(M_1+M_2)$ is the reduced mass of the binary system. In this stage, the evolution of the binary is mainly controlled by the rate at which stars diffuse into the so-called "loss cone". The binary stalls if there are not enough stars that replenish the loss cone.

(4) Gravitational radiation stage: the binary comes into this stage when it becomes sufficiently tightly bound so that GW radiation is the dominant source to drive the orbital decay. For CB-SMBHs with circular orbits, GW radiations shrink the orbital separations on a time scale of (Peters 1964)

$$t_{\rm GW} = \frac{5}{64}\frac{1}{q(1+q)}\frac{R_g}{c}\left(\frac{a}{R_g}\right)^4 \approx 10^6\frac{a_3^4 M_8}{q(1+q)}\ {\rm yr}, \quad (5)$$

where $R_g = GM_1/c^2$.

2.2 Cavity Formation

Artymowicz & Lubow (1994) analytically investigated the gravitational interaction between the binary system with the circumbinary disk (CBD). They showed that the binary is able to create a low-density cavity (also called gap) around the binary because of the Lindblad resonances and make the CBD truncated at an inner edge of $\sim 2a$, with the exact value depending on the mass ratio and eccentricity of the binary. A cavity can be created and maintained if the following two conditions are satisfied: 1) the external torque from the binary exceeds the viscous stresses; and 2) the cavity opening time is shorter than the viscous diffusion time.

For the first condition, the criterion is given by (Lin & Papaloizou 1986)

$$3\pi\alpha\left(\frac{H}{R}\right)^2 \lesssim \frac{T}{\Sigma\Omega^2R^4}, \quad (6)$$

where H/R is the disk aspect ratio, α is viscosity parameter (the ratio of viscous stress to pressure), T is the binary's tidal torque, Σ is the disk's surface density, and Ω is the angular velocity. Decompose the binary's time-periodic gravitational potential into harmonic components and only consider the ($m = 1$) resonance, leading to the mass ratio (see Artymowicz & Lubow 1994 for a detail)

$$q \gtrsim 4\alpha^{1/2}\left(\frac{H}{R}\right)^2 = 10^{-4}\left(\frac{\alpha}{0.1}\right)^{1/2}\left(\frac{H/R}{0.01}\right)^2. \quad (7)$$

For the second condition, the time scale for creating a cavity is (see, e.g., Gültekin & Miller 2012)

$$t_{\rm open} \sim \frac{1}{q^2}\left(\frac{H}{R}\right)^2\left(\frac{\Delta R}{R}\right)^2 t_{\rm Kep}, \quad (8)$$

and the viscous diffusion time is given by

$$t_{\rm close} \sim \frac{(\Delta R)^2}{\nu} = \frac{1}{\alpha}\left(\frac{H}{R}\right)^{-2}\left(\frac{\Delta R}{R}\right)^2 t_{\rm Kep}, \tag{9}$$

where $\nu = \alpha\Omega H^2$ is the viscosity and ΔR is the width of the cavity and the Kepler orbital time is $t_{\rm Kep} = 1/\Omega = 0.5(R/10^3 R_g)^{3/2} M_8$ yr. Requiring $t_{\rm open} \lesssim t_{\rm close}$ results in a similar criterion as Equation (7).

The size of the cavity can be quantitatively estimated by using the approach of Papaloizou & Pringle (1977). Resonant tidal torques from the binary tend to drive gas outward, creating a cavity around the binary. By contrast, viscous torques transport angular momentum outward in the CBD, driving gas to flow inward and refill the cavity. The balance between tidal and viscous torques determines the location of the inner edge of the CBD (Artymowicz & Lubow 1994; Farris et al. 2014). The typical cavity size $\sim 2a$ can be understood from a simple point of view. The dominant resonance occurs at the location with the angular velocity $\Omega = \Omega_{\rm binary}/2$ (Papaloizou & Pringle 1977), corresponding to a radius of $R = 4^{1/3}a \sim 2a$. At the resonance radius, the tidal torque is sufficiently strong to truncate the CBD, within which orbits are dynamically unstable and gas will be cleared out by the binary. The above cavity configuration is confirmed by subsequent numerical simulations (e.g., Artymowicz & Lubow 1994; Artymowicz & Lubow 1996; MacFadyen & Milosavljević 2008; Noble et al. 2012; Shi et al. 2012; Farris et al. 2014). Although the CBDs are truncated, matter still can be supplied to the central binary through gas streams that penetrate the disk cavity without closing it (Artymowicz & Lubow 1996; Shi et al. 2012; Farris et al. 2014; Bowen et al. 2019).

2.3 Geometric Structures of CB-SMBH Systems

There are two fundamental components in CB-SMBH systems: (1) CBDs, and (2) emission line regions. Unlike the situation of a single SMBH, the two components are controlled by the joint potential of the CB-SMBHs. Unfortunately, the configurations have not been fully understood. Roche lobes actually constrain the sizes of the emission line regions, approximated by (Eggleton 1983)

$$\frac{R_{\rm L}}{a} = \frac{0.49q^{2/3}}{0.6q^{2/3} + \ln\left(1 + q^{1/3}\right)}, \tag{10}$$

which is valid for all the mass ratio defined as $q = M_2/M_1$ and $0 < q < \infty$. The broad-line region (BLR) size of each SMBH follows the so-called $R - L$ relation governed by the photoionization process and also depends on the accretion status of SMBHs, which is given by

$$R_{\rm BLR} = 11.6\, \eta_{0.1}^{1/2}\epsilon_{10}^{-1/2}\dot{\mathscr{M}}^{1/2}M_7^{1/2}\ {\rm ltd}, \tag{11}$$

where $M_7 = M_\bullet/10^7 M_\odot$ is the black hole mass, $\eta_{0.1} = \eta/0.1$ is the radiative efficiency, $\epsilon_{10} = \epsilon/10$ is the bolometric correction factor for 5100 Å luminosity (e.g., Bentz et al. 2013; Du & Wang 2019). The dimensionless accretion rate is defined by $\dot{\mathscr{M}} = \dot{M}c^2/L_{\rm Edd}$, where c is the speed of light, $\dot{M}$ is mass accretion rate and $L_{\rm Edd} = 1.4 \times 10^{45}\,M_7\,{\rm erg\,s^{-1}}$ is the Eddington luminosity. Figure 2 shows a schematic for geometric configuration of a CB-SMBH seen in nearly edge-on direction.

3 NUMERICAL SIMULATIONS

There are enormous numerical simulations that are concentrated on CB-SMBH systems using various simulation schemes, such as smooth particle hydrodynamic, purely hydrodynamic, or magnetohydrodynamics (e.g., Artymowicz & Lubow 1994; Artymowicz & Lubow 1996; MacFadyen & Milosavljević 2008; Noble et al. 2012; Shi et al. 2012; Farris et al. 2014; Shi & Krolik 2016; Bowen et al. 2019). Here we only summarize some generic results.

– Numerical simulations confirm the generic binary configuration: a CBD contains a central cavity with a size of $\sim 2a$, as expected from the theoretical consideration (Artymowicz & Lubow 1994; see also Sect. 2). Inside the cavity, gas streams stripped off the inner edge of the CBD directly transport matter onto the binary, forming mini-disks surrounding each black hole. Tidal torques from the binary not only excite density wave near the inner edge of the CBD (Farris et al. 2014), but also truncate the mini-disks with an outer radius smaller than the Roche lobe sizes (Artymowicz & Lubow 1994).
– Numerical simulations found significant periodicity in the accretion rates (e.g., Noble et al. 2012; Shi et al. 2012; Farris et al. 2014; D'Orazio et al. 2015; Bowen et al. 2019). This is generally expected because the binarys orbital motion can modulate accretion processes from the CBD onto the binary black holes. To be specific, the binary's tidal torques excite eccentricity in the cavity and create an overdense lump ($m = 1$ density wave feature dominates) in the inner edge of the CBD. The interaction between the lump and with the passing black holes leads to complex periodicities in the accretion rates to each mini-disk. The dominant period does not always match the orbital period, instead, it depends on the size of the cavity and thus on disk parameters (Farris et al. 2014, 2015; D'Orazio et al. 2015; Bowen et al. 2019). As D'Orazio et al. (2015) summarized, numerical simulations generally found that for $0.05 \lesssim q \lesssim 0.3$, the accretion rate variations

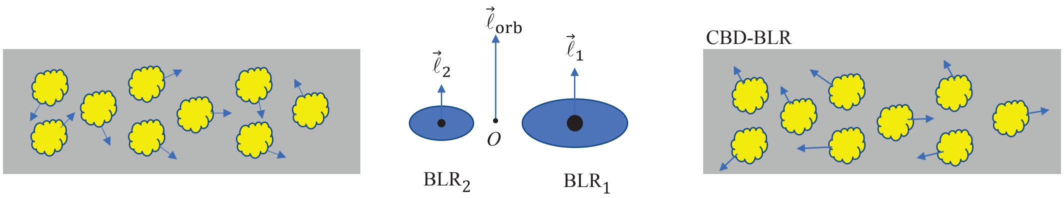

Fig. 2 A configuration of a CB-SMBH seen in nearly edge-on direction. $\ell_{1,2}$ and $\ell_{\rm orb}$ represent the angular momentum directions of the primary, secondary, and the binary, respectively. Arrows of clumps in the CBD-BLR represent random motion. O is the mass center of the binary, and the arrows represent the directions of angular momentum of BLRs and the binary orbit. There are likely three broad-line regions: BLR$_1$ surrounding the primary and BLR$_2$ the secondary, and the CBD-BLR around the binary. The CBD is a vertically self-gravitating disk. In this configuration we assume the simplest case where BLRs, the binary orbit and CBD are co-planar. However, the random motion of CBD clouds allows random tidal capture of each SMBH and BLRs have random directions accordingly.

have a period of $P_{\rm orb}$, with an additional period at $0.5P_{\rm orb}$; for $0.3 \lesssim q \lesssim 0.8$, the main period is that of the overdense lump, roughly equal to $(3-8)P_{\rm orb}$, with additional periods at $0.5P_{\rm orb}$ and $P_{\rm orb}$; for equal-mass binaries, the variations are dominated by longer lump period together with $0.5P_{\rm orb}$.

– Streams of gas are efficiently peeled off from the inner edge of the CBD, pass through the cavity, and feed the persistent mini-disks surrounding each black hole. The accretion rates onto each black hole are different, depending on the mass ratio and eccentricity of the binary (e.g., Farris et al. 2014; Bowen et al. 2019). The secondary black hole generally has a relatively larger accretion rate than the primary because it can reach closer to the inner edge of the CBD (Hayasaki et al. 2008; Roedig et al. 2012; Farris et al. 2014). The gas streams may impact on the mini-disks, creating shocks and hot spots in the mini-disks (Shi et al. 2012). Because stream impact is periodic, the resulting flares from shocks and hot spots may be also periodic.

The above results were obtained upon prograde CBDs, namely, the rotation axes align with those of the binaries. Alternatively, it is possible that CBDs rotate retrogradely. The behaviors of retrograde CBDs are fundamentally different compared to their prograde counterparts, because of the absence of orbital resonances (Nixon et al. 2011). This can be simply understood as follows. Tidal interaction occurs mainly through resonances at the location where the angular velocity Ω satisfies (Papaloizou & Pringle 1977)

$$\Omega^2 = m^2(\Omega - \Omega_{\rm bin})^2, \tag{12}$$

where $\Omega_{\rm bin}$ is the binary's orbital frequency and $m = 1, 2, ...$ is the wave mode number. In retrograde CBDs, Ω and $\Omega_{\rm bin}$ have opposite signs so that the above equation no longer holds. In other words, there are no resonant regions in retrograde CBDs (however, see also Nixon & Lubow 2015 for eccentric binary orbits). This property is also confirmed by the numerical simulation of Bankert et al. (2015). As a result, there are no cavities developed within the retrograde disks and matter can be directly accreted from the disks onto the binaries. For the same reason, retrograde CBDs also do not develop prominent lumps near the inner edges seen in prograde disks (Bankert et al. 2015).

An important implication of retrograde CBDs is that the negative orbital angular momentum of the accreted gas can directly reduce the binary's angular momentum and therefore expedite the binary's dynamical evolution to GW radiation dominated stage. This may provide a possible solution to the final parsec problem (Nixon et al. 2011; Nixon & Lubow 2015). For the sake of simplicity, if we assume that all mass is accreted into the secondary black hole so that all of the negative angular momentum is transferred to the secondary, the orbital separation of a circular binary evolves after a mass increasement of ΔM for the secondary follows (Nixon et al. 2011)

$$\frac{\Delta a}{a} = -4\left(\frac{\Delta M}{M_2}\right). \tag{13}$$

As can be seen, the orbital separation $a \propto M_2^{-4}$, indicating that a rapid growth of the secondary can significantly shrink the binary's orbit.

In addition, numerous simulations also show that gas-rich environments can efficiently absorb and transfer the orbital angular momentum through the tidal interaction with the prograde CBD (Escala et al. 2005; MacFadyen & Milosavljević 2008; Cuadra et al. 2009; Lodato et al. 2009), or the retrograde CBD (Goicovic et al. 2017, 2018). Such a configuration of accretion onto binary black holes has been found in NGC 1068 by ALMA (Impellizzeri et al. 2019), which provides a unique opportunity to investigate the orbital evolution predicted by simulations.

4 OBSERVATIONAL FEATURES

The suggested signatures so far include (but not limited to): (1) shifts of red and blue peaks of broad emission lines in long-term variations similar to the cases in normal binary stars; (2) deficit profiles of brightness of galactic centers as a result of ejection of stars through interaction of stars with the binary black holes; (3) periodicity of long-term variations of AGNs from a few years to a few tens of years, which is regarded as results of modulation of the orbital motion of CB-SMBHs; (4) continuum deficits arising from the central cavity of the CBD governed by the tidal torques of the binary; (5) two-dimensional kinematic maps of broad emission lines in AGNs showing signatures of two point potentials through reverberation mapping campaigns; (6) spectroastrometry with GRAVITY (or Extremely Large Telescope: ELT) may reveal some signals of double BLRs; (7) gas dynamics of CBDs with long-standing counter rotations; (8) unique features in polarized spectra; and (9) changing-look AGNs with peculiar flux variations. Additionally, X-shaped radio jet was also regarded as a signature of CB-SMBHs (Merritt & Ekers 2002), but it hardly applies to measure orbital parameters of the binaries. Below we briefly mention about the first two signatures and discuss the rest signatures in more depth.

4.1 Shifting of Broad Emission Lines

CB-SMBH systems could contain very complicated BLRs and the real situation is far from understanding. Figure 2 shows the simplest case of BLR configurations in CB-SMBHs. The BLR components surrounding each black hole have line shifts due to orbital motion of the binary, while the CBD-BLR component has a relatively narrower and stable line profile (if it exists). In reality, the situation is by no means such simple. First, it is fully uncertain whether the CB-SMBH orbit is coplanar (or anti-coplanar) with the CBD. Second, how many BLR components are there in a CB-SMBH system? This issue probably depends on the binary separations and orbital eccentricities. In the literature, it is usually assumed that there are two BLRs (Popovic et al. 2000; Shen & Loeb 2010; Wang et al. 2018). In addition, long-term campaigns of searching for CB-SMBHs make an attempt to capture spectral features predicted by the scheme of binary BLRs. As we will show below, reverberation mapping campaigns are able to detect binary signals through measuring the geometry and kinematics of ionized gas in galactic centers.

On the other hand, searching for periodic shifts of double-peaked profiles in AGNs is expected to indicate CB-SMBHs (Runnoe et al. 2017; Doan et al. 2020; Guo et al. 2019). Similar to classical binary stars, the double BLRs orbiting around each black hole will lead to opposite shifts of the red and blue peaks along orbital phases. A long term monitoring campaign is being conducted by Eracleous et al. (2012) for a sample of AGNs, in which SDSS J0938+0057, SDSS J0950+5128, and SDSS J1619+5011 showed systematic and monotonic velocity changes consistent with the binary hypothesis (Runnoe et al. 2017). A possible issue about this approach is that BLRs may have dynamical evolution over years, which causes extra shifting of broad emission lines and therefore contaminates the shifting due to the binary's orbital motion.

4.2 Mass Deficits in Density Profiles of Galaxy Nucleus

As a consequence of interaction with CB-SMBHs, stars are ejected from galactic center, forming a "mass deficit" in its central part as revealed by numerical simulations (Ebisuzaki et al. 1991; Milosavljević et al. 2002; Merritt 2006). Actually, it does not appear to have a pronounced and unambiguous detectable effect on the density profile. Even though it works for searching for CB-SMBHs, this method cannot determine orbital parameters of the binary to test GW properties. The same shortcomings pertains to the identifications of AGNs with X-shaped jet morphology.

4.3 Periodicity of Long-term Variations

Periodic brightness variability in long-term monitoring of AGNs has been widely used to search for CB-SMBH candidates in modern time-domain surveys (e.g., Graham et al. 2015a; Charisi et al. 2016; Liu et al. 2019). To date, systematic searches from large surveys have yielded more than one hundred quasar and AGN candidates with periodic variability, distributed over a wide redshift range up to $z \sim 3$. Among those candidates, PG 1302-102 is the presently best one with a period of 5 yr (Graham et al. 2015a; D'Orazio et al. 2015). The number of candidates will certainly grow explosively with forthcoming large time-domain surveys brought into operation (such as the Zwicky Transient Facility, Bellm et al. 2019; the Large Synoptic Survey Telescope, Ivezic et al. 2008). There are also a number of quasars and nearby AGNs that were reported individually to exhibit periodicity based on long-term databases (see Table 1), including (but not limited to) OJ 287 with a period of about 12 yr over a century of data (Valtonen et al. 2008), NGC 5548 with a period of about $\sim$ 13 yr over 40 yr (Li et al. 2016; Bon et al. 2016), and Akn 120 with a period of $\sim$ 20 yr over the last 40 yr (Li et al. 2019). In addition, there are a few periodic AGN candidates reported in γ-ray light curves over the Fermi Large Area Telescope source catalog (e.g., Zhang et al. 2020 and references therein). Albeit with these progresses, we keep in mind that, due to the limited temporal baselines, the time series data generally cover only a few cycles of the detected periods. This raises a serious concern over the false positive detection of periodicity, given that aperiodic, red-noise AGN variability can easily produce spurious few-cycle periodicities (Vaughan et al. 2016). Either sophisticated period searching algorithms or longer data baselines are needed to rule out spurious periodic signals.

Meanwhile, as mentioned above, numerical simulations found that the periods in mass accretion rates onto the binary do not always match the orbital period (Farris et al. 2014; D'Orazio et al. 2015). This means that one should treat with caution the observed periods in flux variability if particularly using the periods to derive other binary's properties.

4.4 Continuum Deficits

The presence of a low-density cavity between the CBD and the mini accretion disks around each black hole implies that there is little amount of emissions from the cavity, resulting in a dip in the thermal continuum spectrum emitted by the system. This feature was noticed by Gültekin & Miller (2012) and then further investigated by several studies, among which include Sesana et al. (2012), Tanaka & Haiman (2013), Roedig & Sesana (2014), and Yan et al. (2014). The characteristic wavelength of the dip can be estimated by (Gültekin & Miller 2012)

$$\lambda_0 \approx 140 \left(\frac{R_{\rm cav}}{R_g}\right)^{3/4} \left(\frac{\dot{\mathscr{M}}}{0.1}\right)^{-1/4} M_8^{1/4}\,\text{Å}, \qquad (14)$$

where $R_{\rm cav} \sim 2a$ is the size of the cavity. As can be seen, the wavelength λ_0 of the deficit lies at from UV/optical to IR bands, depending the orbital separation and total mass of the binary and accretion rate of the CBD. Figure 3 shows examples of spectral energy distributions with cavities, adapted from Sesana et al. (2012).

The first candidate for such a continuum deficit was proposed by Yan et al. (2015) upon the quasar Mrk 231, which shows a distinctly red optical-to-UV spectrum with a sharp drop off and flux deficit at $\lambda \sim 4000 - 2500$ Å. Yan et al. (2015) used a binary scenario to interpret the optical-to-UV spectrum and from which, the orbital parameters of the binary can be determined. However, the binary hypothesis was debated by Leighly et al. (2016) and Veilleux et al. (2016). Recently, Guo et al. (2020) compiled spectral energy distributions (SEDs) of candidate periodically variable quasars and found that compared to control quasar sample matched in redshift and luminosity, those candidate periodic quasars do not show distinct SEDs. In generic, dust reddening may cause red SEDs, making the search for continuum deficit much challenging. Moreover, it has been shown that the binary black holes are

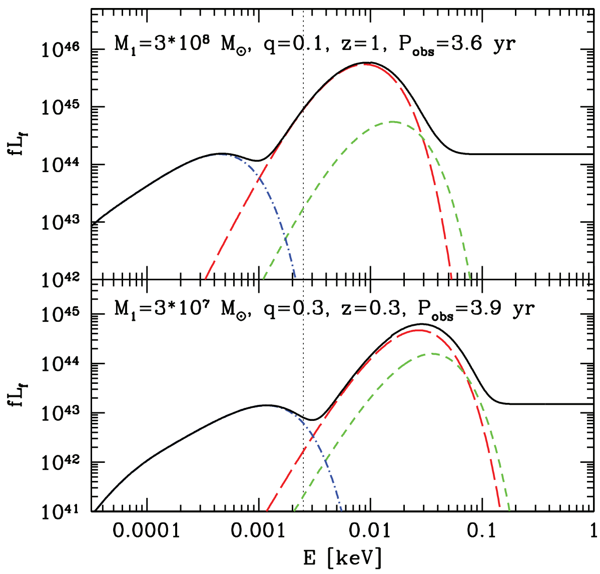

Fig. 3 Examples of spectral energy distributions with cavities. The dot-dashed blue lines, long dashed red lines, and short dashed green lines represent thermal emissions from the CBD, mini-disks of the primary and secondary, respectively. We note that a flat X-ray emission from a putative hot corona is added, leading to a flat spectrum beyond ~ 0.1 keV. Adapted from Sesana et al. (2012).

peeling off gas from the inner edge, which penetrate the cavity (Farris et al. 2014; Shi & Krolik 2016; Bowen et al. 2019). These gas streams may also contribute thermal emissions that blur the deficit.

4.5 Reverberation Mapping: Spatial Resolution from Time Domain

Reverberation mapping (RM) of AGNs is a powerful tool to probe the kinematics and structure of BLRs (Peterson 1993). In principle, the kinematics of broad-line gas is governed by the central black hole's potential, and therefore it is expected to exhibit signatures of CB-SMBH orbital motion, which can be diagnosed from the two-dimensional velocity delay map (Wang et al. 2018; Songsheng et al. 2020; Kovačević et al. 2020). The advantage of this approach is obvious: campaigns can be performed in seasons and long-term monitoring is not required as for the approach of period searching. A campaign called Monitoring AGNs with Hβ Asymmetry (MAHA) has been conducted with Wyoming Infrared Observatory (WIRO) Telescope, which, as the name implies, mainly monitors AGNs with asymmetric Hβ profiles (Du et al. 2018).

The velocity delay map Ψ of BLRs is defined through the following equation

$$L_\ell(v,t) = \int \Psi(v,\tau) L_c(t-\tau) d\tau, \qquad (15)$$

where L_ℓ and L_c are the light curves of the emission line and continuum, respectively.

For a CB-SMBH system, we suppose that there are binary BLRs and they are independently photoionized only by disk emissions of their own black holes (their CBDs are neglected which mainly emits optical/IR photons). We denote this systems as detached CB-SMBHs. Two ionizing continuum sources $L_{1,2}^{\rm c}(t)$ are independently varying and $L_{1,2}^{\ell}(v,t)$ are the response variations of the broad emission lines. Since CB-SMBHs are usually spatially unresolved, we only observe the total fluxes of emission lines and continuum. The total velocity delay map (or transfer function) of the binary BLRs can be expressed by

$$\begin{aligned}\Psi_{\rm tot}(v,t) &= \mathscr{F}^{-1}\left[\frac{\tilde{L}_1^{\ell}(\omega)+\tilde{L}_2^{\ell}(\omega)}{\tilde{L}_1^{\rm c}(\omega)+\tilde{L}_2^{\rm c}(\omega)}\right]\\ &= \mathscr{F}^{-1}\left[\frac{\mathcal{L}_1(\omega)}{1+\Gamma_\omega}+\frac{\mathcal{L}_2(\omega)}{1+\Gamma_\omega^{-1}}\right],\end{aligned} \tag{16}$$

where $\mathscr{F}^{-1}$ is the inverse Fourier transform, the tilde symbol represents the Fourier transform of the corresponding light curve, $\mathcal{L}_{1,2}(\omega)=\tilde{L}_{1,2}^{\ell}(\omega)/\tilde{L}_{1,2}^{\rm c}(\omega)$, and $\Gamma_\omega=\tilde{L}_2^{\rm c}(\omega)/\tilde{L}_1^{\rm c}(\omega)$ indicates a coupling between continuum variations in the frequency space calculated by the Fourier transform. The above equation demonstrates the variation-coupling effect and Γ_ω is a key parameter determined by the properties of the continua associated with each of the binary black holes. Given the emissivity distribution $\epsilon(\boldsymbol{R})$ based on the geometries of the BLR and the projected velocity distribution $g(\boldsymbol{R},v)$, we have

$$\Psi_{\rm tot}(v,t)=\sum_{k=1}^{2}\int d\boldsymbol{R}_k\,\mathcal{H}_k(v,\boldsymbol{R}_k)\mathcal{Q}_k(v,t,R_k), \tag{17}$$

where $\mathcal{H}_k(v,\boldsymbol{R}_k)=\epsilon(\boldsymbol{R}_k)g(\boldsymbol{R}_k,v)/4\pi R_k^2$, and

$$\mathcal{Q}_{1,2}(v,t,R_{1,2})=\frac{1}{2\pi}\int_{-\infty}^{+\infty}d\omega\left[\frac{e^{-i\omega t_1}}{1+\Gamma_\omega},\frac{e^{-i\omega t_2}}{1+\Gamma_\omega^{-1}}\right], \tag{18}$$

where the subscripts correspond to the first and the second terms in the mid-bracket, respectively, and $t_{1,2}=t-(R_{1,2}+\boldsymbol{R}_{1,2}\cdot\boldsymbol{n}_{\rm obs})/c$, $\boldsymbol{n}_{\rm obs}$ is the observer's line of sight and c is the speed of light.

In a single BLR, $\mathcal{Q}_{1,2}\equiv\delta(t')/2$ with $t'=t-(R+\boldsymbol{R}\cdot\boldsymbol{n}_{\rm obs})/c$ leads to a simple expression (Blandford & Mckee 1982), where $\delta(t')$ is the δ-function. We stress that the total TF is not a simple summation of two individual functions as shown by Equations (17, 19) due to $\mathcal{Q}_{1,2}$. Actually, $\mathcal{Q}_{1,2}$ indicates a coupling between the AGN continuum variability patterns, arising from the spatially unresolved effect of the binary black holes.

In principle, Γ_ω is not well known from accretion-disk theories. The simplest case is that the double black holes have the same properties of continuum variations, i.e. they approximately have same power spectral density. In such a case, we have $\Gamma_\omega\approx\Gamma_0=\text{constant}$, yielding the following formulation from Equation (17)

$$\Psi_{\rm tot}(v,t)=\frac{\Psi_1(v,t)}{1+\Gamma_0}+\frac{\Psi_2(v,t)}{1+\Gamma_0^{-1}}, \tag{19}$$

where

$$\Psi_{1,2}(v,t)=\int d\boldsymbol{R}_{1,2}\,\mathcal{H}_{1,2}(v,\boldsymbol{R}_{1,2})\delta(t_{1,2}), \tag{20}$$

are the 2D-TFs of each BLR. Monte-Carlo simulations by (Songsheng et al. 2020) showed that Equation (19) generally holds for AGN variations (following the damped random walk model). The parameter Γ_0 cannot be $\Gamma_0\gg1$ or $\Gamma_0\ll1$ to avoid cases in which one of the binary BLRs dominates over the other. The present scheme for CB-SMBHs is only valid for $\Gamma_0\sim1$, likely for high mass ratio systems. Figures 4 and 5 show examples of 2D-TFs for BLRs surrounding a single SMBH and a CB-SMBH, respectively.

4.6 Interferometric Signals from Spatially Resolved Structure

"Differential Speckle Interferometry" as the progenitor of the spectroastrometry was first suggested by J. M. Beckers (Beckers 1982) and its feasibility was demonstrated by R. Petrov (Pérol 1998). Spectroastrometry is a powerful tool with high spatial resolution. Given the surface brightness distribution of a BLR, we have the photocenter of the source as a function of wavelength

$$\boldsymbol{\epsilon}(\lambda)=\frac{\int\boldsymbol{\alpha}\mathcal{O}(\boldsymbol{\alpha},\lambda)\,{\rm d}^2\boldsymbol{\alpha}}{\int\mathcal{O}(\boldsymbol{\alpha},\lambda)\,{\rm d}^2\boldsymbol{\alpha}}, \tag{21}$$

where $\mathcal{O}(\boldsymbol{\alpha},\lambda)=\mathcal{O}_\ell+\mathcal{O}_{\rm c}$ is the surface brightness distribution of the source contributed by the BLR and continuum regions, respectively, and $\boldsymbol{\alpha}$ is the angular displacement on the celestial sphere. Given the geometry and kinematics of a BLR, its $\mathcal{O}_\ell$ can be calculated for one broad emission line with the observed central wavelength $\lambda_{\rm cen}$ through

$$\mathcal{O}_\ell=\int\frac{\Xi_r F_{\rm c}}{4\pi r^2}f(\boldsymbol{r},\boldsymbol{V})\delta(\boldsymbol{\alpha}-\boldsymbol{\alpha}')\,\delta(\lambda-\lambda')\,{\rm d}^3\boldsymbol{r}\,{\rm d}^3\boldsymbol{V}, \tag{22}$$

where $\lambda'=\lambda_{\rm cen}\gamma_0\left(1+\boldsymbol{V}\cdot\boldsymbol{n}_{\rm obs}/c\right)\left(1-R_{\rm S}/r\right)^{-1/2}$ includes gravitational redshifts due to the central black hole, $\gamma_0=\left(1-V^2/c^2\right)^{-1/2}$ is the Lorentz factor, $\boldsymbol{\alpha}'=\left[\boldsymbol{r}-\left(\boldsymbol{r}\cdot\boldsymbol{n}_{\rm obs}\right)\boldsymbol{n}_{\rm obs}\right]/D_{\rm A}$, $\boldsymbol{r}$ is the displacement to the central black hole, Ξ_r is the reprocessing coefficient at position $\boldsymbol{r}$, $f(\boldsymbol{r},\boldsymbol{V})$ is the velocity distribution of BLR clouds, $F_{\rm c}$ is ionizing fluxes received by an observer, and $\boldsymbol{n}_{\rm obs}=(0,\sin i_0,\cos i_0)$ is the unit vector pointing from the observer to the source. Introducing the fraction

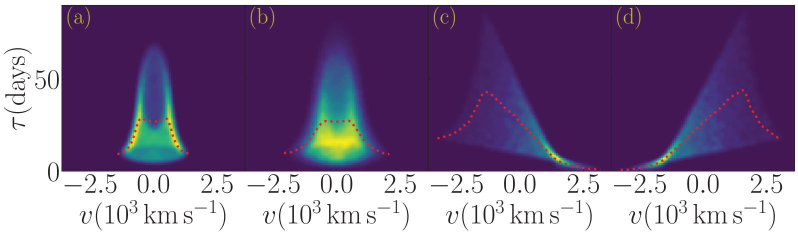

Fig. 4 Examples of 2D-TFs for a single BLR with different geometries, with red lines corresponding to the (v, τ)-planes. In panels (a) and (b): $\Theta_{\rm disk} = (5^\circ, 30^\circ)$ represent geometrically thin and flattened disks; (c) and (d): $\Theta_{\rm flow} = 45^\circ$ is for inflows/outflows. We took $(\alpha_0, \alpha; \beta_0, \beta; \gamma_{1,2,3}) = (1.4, 0; 1.6, 0.1; 0.5)$, $M_\bullet = 10^7 M_\odot$, $(R_{\rm in}, R_{\rm out}) = (9, 45)$ltd and $i_0 = 30^\circ$. For a disk $R_{\rm mid} = R_{\rm out}$ and for inflows and outflows $R_{\rm mid} = R_{\rm in}$. Adapted from Wang et al. (2018).

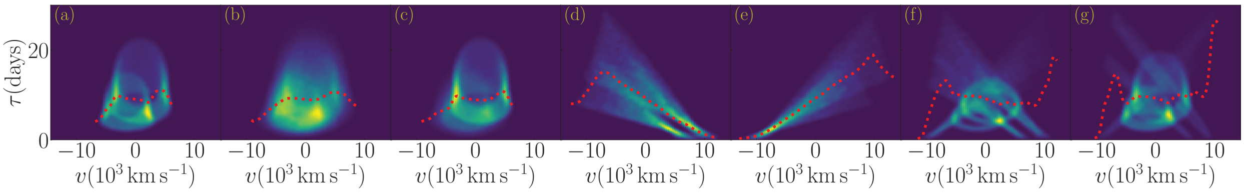

Fig. 5 Examples of 2D-TFs for compositions of same kinds of BLR geometries and the corresponding (v, τ)-plane (red lines) with $(i_0, \phi_0) = (30^\circ, 150^\circ)$. $(\epsilon_{1,2,3}; \gamma_{1,2,3}; \alpha_0, \alpha; \beta_0, \beta)$ are the same with a single BLR. Panel *a* is for 2⊗thin-disks; *b*: 2⊗thick-disks; *c*: (thin⊗thick)-disks; *d*: 2⊗inflows; *e*: 2⊗outflows; *f*: 2⊗(thin-disk+inflows+outflows) with smaller $R_{\rm mid}$, but *g*: with larger $R_{\rm mid}$. Generally, they are different from a single AGN. Here the symbol ⊗ represents a composition of one binary system. Adapted from Wang et al. (2018).

of the emission line to total (ℓ_λ) and assuming that the photocenter of $\mathcal{O}_{\rm c}$ is zero, we have

$$\boldsymbol{\epsilon}(\lambda) = \ell_\lambda\, \boldsymbol{\epsilon}_\ell(\lambda), \tag{23}$$

where

$$\boldsymbol{\epsilon}_\ell(\lambda) = \frac{\int \boldsymbol{r}\mathcal{O}_\ell\, {\rm d}^2\boldsymbol{\alpha}}{\int \mathcal{O}_\ell\, {\rm d}^2\boldsymbol{\alpha}},$$
$$\ell_\lambda = \frac{F_\ell(\lambda)}{F_{\rm tot}(\lambda)},$$
$$F_\ell(\lambda) = \int \mathcal{O}_\ell\, {\rm d}^2\boldsymbol{\alpha}\,,$$
$$F_{\rm tot}(\lambda) = F_\ell(\lambda) + F_{\rm c}(\lambda).$$

For an interferometer with a baseline $\boldsymbol{B}$, a non-resolved source with a global angular size smaller than its resolution limit λ/B has the interferometric phase

$$\phi_*(\lambda, \lambda_{\rm r}) = -2\pi\boldsymbol{u}\cdot[\boldsymbol{\epsilon}(\lambda) - \boldsymbol{\epsilon}(\lambda_{\rm r})], \tag{24}$$

where $\boldsymbol{u} = \boldsymbol{B}/\lambda$ is the spatial frequency and $\lambda_{\rm r}$ is the wavelength of a reference channel.

GRAVITY/VLTI provides the highest spatial resolution in NIR. For $B/\lambda \sim 100\,{\rm m}/2.2\,\mu{\rm m}$ and $\epsilon \sim 100\,\mu{\rm as}$, ϕ_*-amplitudes are expected to be at a level of a few degrees. The differential phase curves measured by GRAVITY depends on the geometric structures and kinematics of BLRs. Figure 6 shows several panels of single BLRs with different parameters for GRAVITY/VLTI signals. In cases of CB-SMBHs, there are several simplest configurations of angular momentum distributions of individual BLRs and binary orbital motion. Details of the phase curves have been explored by Songsheng et al. (2019). See Figure 7 for four simplest configurations of CB-SMBHs, and compare them with Figure 6 for differences of single and binary BLRs. However, it is worth mentioning that the BLRs in CB-SMBHs are highly uncertain even in theoretical points of view.

4.7 Gas Dynamics of Circumbinary Disks

There is growing evidence for random fueling from the circumnuclear regions to the central black hole (Tremblay et al. 2016; Temi et al. 2018). The high quality SINFONI/VLTI observations of NGC 1068 show two oppositely moving tongues around the center within a few parsec (Müller Sánchez et al. 2009). It is then expected that there must be cases with counter rotating disks (CRDs) within 10 parsec regions. The CRD fates fully depend on the central dynamical engines: (1) a single SMBH; and (2) CB-SMBHs. For the first case, the CRD is suffering the well-known Kelvi-Helmholtz instability (KHI) within the Keplerian timescale, providing a very efficient way to increase the SMBH mass (Quach et al. 2015; Dyda et al. 2015). For the second case, the tidal torques of the CB-SMBHs supply angular momentum to support the CRD avoiding the KHI catastrophe (Wang et al. 2020).

Recently, the observations of the Atacama Large Millimeter/submillimeter Array (ALMA) discovered such a counter rotating gas disk between 0.1–7 parsec (Impellizzeri et al. 2019). Interestingly, there is a counter rotating disk at a scale of 100 parsec (Imanishi et al. 2018).

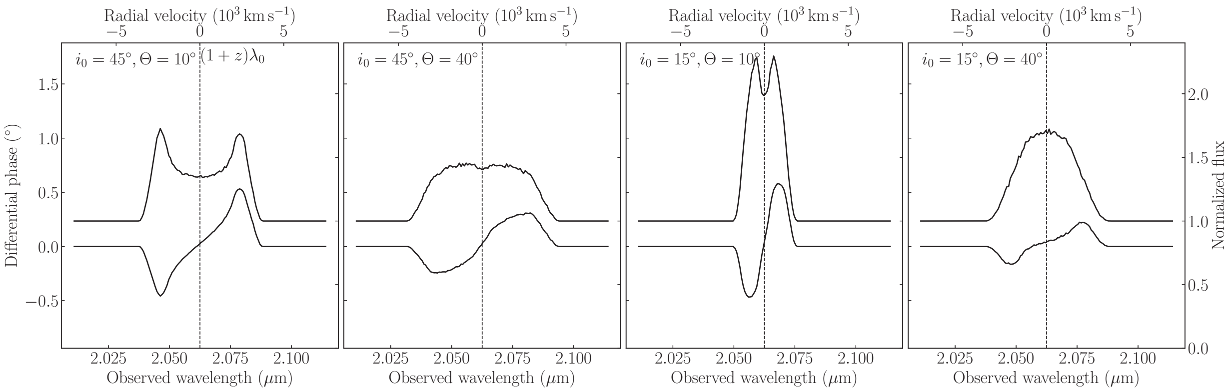

Fig. 6 Line profiles (*upper lines*) of a singe disk BLR and differential phase curves (lower lines) for different inclinations and thickness. The differential phase curves are regarded as the S-shape changing with inclinations and thickness of the BLR, but the S-shape always appears whatever the line profile is double or single peaked. Adapted from Songsheng et al. (2019).

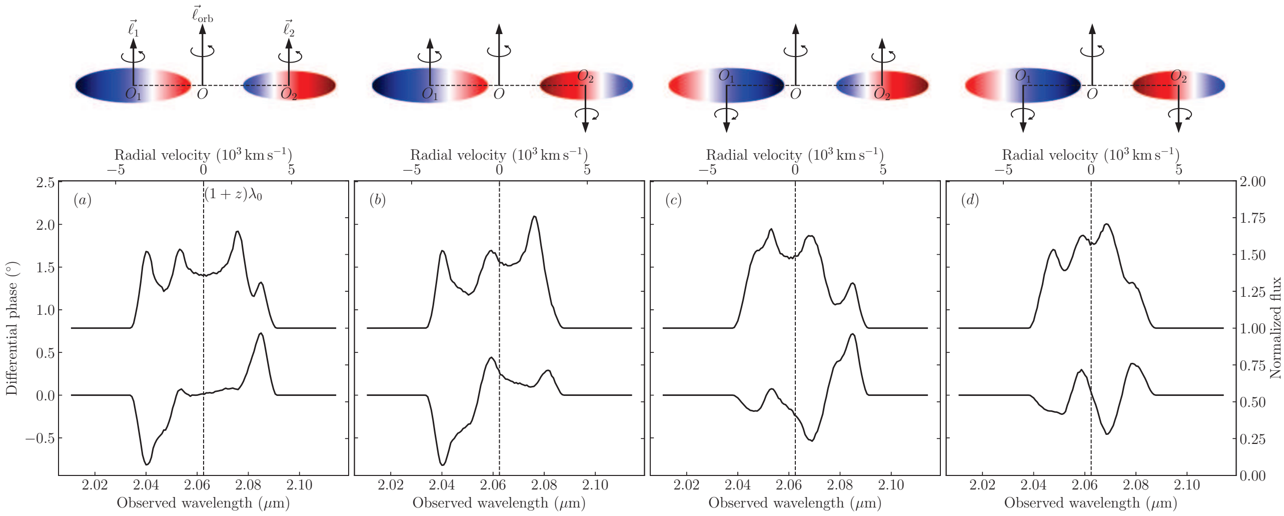

Fig. 7 Line profiles (*upper lines*) of binary thin disk BLRs and differential phase curves (*lower lines*) of the four simplest groups in light of combinations of angular momentum. Adapted from Songsheng et al. (2019).

Considering that the lifetime of NGC 1068 CRD is much longer than the Keplerian timescale, external supply of angular momentum to the CRD is necessary. Wang et al. (2020) show that this external source is a CB-SMBH with a total mass of $2 \times 10^7 M_\odot$ and a mass ratio of about $q = 0.3$. Orbital period is about 870 yr. Figure 8 shows a carton of CB-SMBHs in NGC 1068. Gravitational waves from NGC 1068 is very weak since the merger timescale is longer than the Hubble time. On the other hand, this hypothesis of CB-SMBHs in NGC 1068 should be tested independently from observations, such as dynamics of the maser disk (e.g., Greenhill & Gwinn 1997). Detailed dynamical modeling of the maser or molecular gas at parsec scales will allow us to determine some of the orbital parameters.

Retrograde accretion onto CB-SMBHs is an efficient way of cancelling orbital angular momentum of the binary system (e.g., Roedig & Sesana 2014), and therefore of alleviating the "final parsec problem". Fortunately, the ALMA observations of molecular gas in the CRD allow us to estimate about orbital evolution of the binary. It is found that the CRD can drive the binary black holes into GW-driven stage about four times fast. ALMA observations of local Seyfert galaxies have been conducted (Combes et al. 2019), but surveys have not been carried out for a systematic search of CB-SMBHs.

Additionally, the KHI releases a huge amount of energy due to friction between the CRDs. The KHI layer is formed with strong shocks giving rise to emission from radio to γ-ray. Soft-rays produced in the KHI layer is stable, but is absorbed by the obscuring torus since it is an edge-on source. We hope to detect more similar CRDs in Seyfert galaxies. Moreover, shocks efficiently accelerate electrons so that inverse Compton scattering significantly generates γ-rays at GeV band. Indeed, *Fermi*-observations already detected γ-rays in NGC 1068. Though the $\gamma-$rays in NGC 1068 are currently explained by star formation in the CNR, γ-ray emissions are an appealing feature of the KHI layer of CRD systems. It is expected to spatially resolve γ-ray regions from CRDs by future γ-ray detectors. The present suggestion of a CB-SMBH residing in NGC 1068 can then be finally tested, see details in Wang et al. (2020).

4.8 Signals from Polarized Spectra

Supposing that there are two BLRs in the CB-SMBHs wrapped in the dusty torus, what are signals from the polarized spectra? To understand the complicated results of binary BLRs, we recall the properties of polarized spectra of AGNs containing one single SMBH. The polarized spectra mainly depend on spatial distributions of scattering electrons. Generally, there are two first-scattering regions. The first region corresponds to electrons located in the equatorial plane and the second region is polar electron screen above the BLR (roughly $\sim\,0.1\,$kpc) (Smith et al. 2005). The scattering in the second region is usually much weaker than in the first region because of the very small scattering depth. The real distributions of scattering electrons could be a kind of hybrid configurations of pole and equatorial regions.

For type-1 AGNs, scattering from the equatorial regions dominates so that the polarized spectra in effect correspond to the intrinsic spectra observed in the mid-plane, namely, edge-on spectra. It is then expected to see double-peaked polarized spectra for a single BLR. For co-planar BLRs around CB-SMBHs, the polarized spectra will be multiple-peaked. The spectra will be much more complicated for mis-aligned binary BLRs. For type-2 AGNs, however, observers receive the BLR photons polarized by electrons located in polar regions, and in effect see the face-on spectra, likely simpler than for type-1 AGNs.

Savić et al. (2019) had made the first effort through the Monte Carlo code STOKES to solve 3D polarized radiative transfer for signals of CB-SMBHs with different kinematics and geometries. They included several configurations: 1) two separate BLRs; 2) partially merged BLR; and 3) two spiral arms inside the cavity of the CBD. They found that the polarization position angle shows quite different and unique profiles from single SMBH cases. It is expected that spectropolarimetry could be an effective tool to search for candidates based on some features of CB-SMBHs appearing in the polarized spectra and thereby deserves further detailed investigations.

4.9 Changing-look AGNs

It is well-known that AGNs are usually classified into type-1 and type-2 according to visibilities of broad emission lines. There are also intermediate types quantitatively defined as

$$N_{\rm type}=1+\left(\frac{F_{\rm nl}}{F_{\rm tot}}\right)^{0.4}, \tag{25}$$

where $F_{\rm nl}$ and $F_{\rm tot}$ are the narrow and total (broad and narrow) line fluxes (Cabell et al. 1992). Generally $N_{\rm type}\lesssim 1.5$ AGNs are referred to type-1 and otherwise type-2. The two classes can be unified by obscurations of a dusty torus (hydrogen column density $N_{\rm H}\gtrsim 10^{22}\,{\rm cm}^{-2}$) orientated differently relative to observers, which is evidenced by polarized spectra of type-2 AGNs appearing normal broad Balmer lines (Antonucci & Miller 1985; Antonucci 1993). This scenario receives much success during the last 30 years (Netzer 2015).

However, there are several outliers showing a fast transition between type-1 to -2, such as NGC 3516, NGC 4151, Fairall 9 and 3C 390.3. This is in conflict with the orientation unification scenario considering that orientations are not expected to have fast changes. From time-domain surveys, evidence is ever growing for transitions of AGN classifications between type-1 and type-2 (MacLeod et al. 2016, 2019). The type transitions are fast so that it is hard to reconcile with any known timescales of accretion physics (e.g., Ross et al. 2018). It turns out that the transition cannot be governed by changes of obscurations from polarization observations (Hutsemékers et al. 2019; Marin et al. 2019). Those AGNs undergoing type transitions are nowadays called changing-look AGNs (CL-AGNs). How to rapidly quench accretion onto SMBHs to make a transition remains a big puzzle. It is quite clear, however, that *external* torques must be invoked.

Recently, Wang & Bon (2020) suggested that type transitions could be driven by tidal torques of the companion at the periastron in systems of binary SMBHs. In a close binary system with high eccentric orbit, the periastron duration is about $t_{\rm peri}\approx(1-e)^{3/2}P_{\rm orb}\lesssim 0.03P_{\rm orb}$ for $e\gtrsim 0.9$ and mini-disks are built up at the apastron through peeling off gas from the inner edge of the CBD. However, the mini-disks are strongly affected by the tidal interaction with the companion SMBHs. Tidal torques completely change accretion status of the disks. Considering the complicated process supplying gas, we focus on four simplest configurations as plotted in Figure 9. Tidal torques due to companion SMBHs drive the fates of the mini-disks, depending on the angular momentum

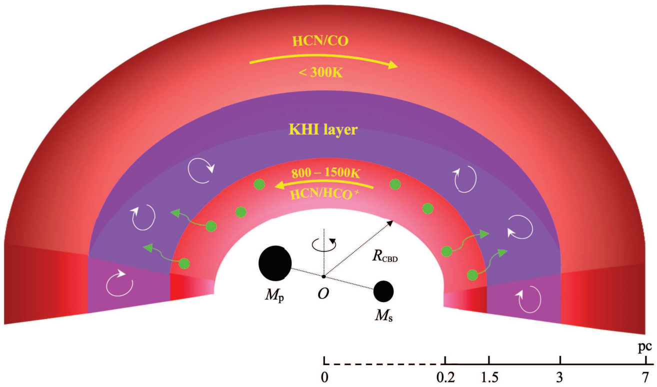

Fig. 8 A carton of CB-SMBHs in the Seyfert 2 galaxy NGC 1068. High spatial resolution ALMA observations of molecular emission lines (CO and HCN) reveal two counter rotating disks (CRDs) with Keplerian rotation velocity within 7 parsec separated by ~ 3 pc. This is the first Seyfert galaxy with a CRD. Likely, the unique mechanism supporting the CRD is the tidal torque of CB-SMBHs. It is expected to detect such CRDs in Seyfert 1 galaxies. Adapted from Wang et al. (2020).

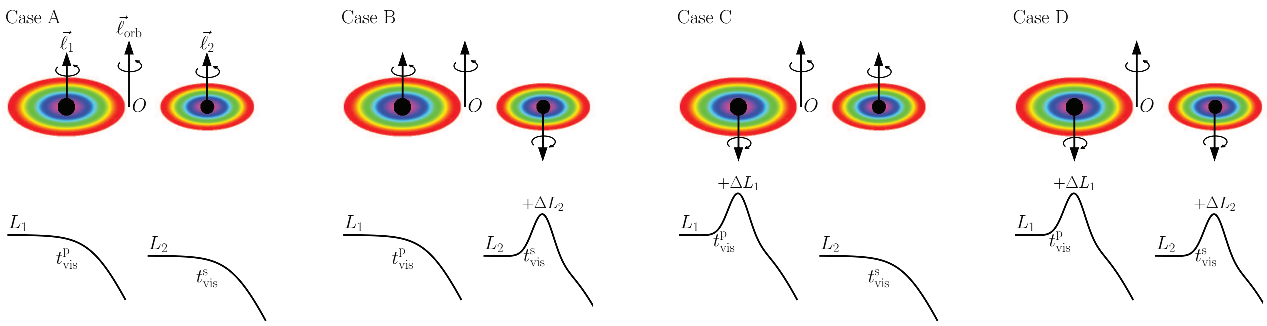

Fig. 9 A sketch for changing-look AGNs. Type transitions are driven by tidal interaction between the mini-disks and its companion black hole. O is the mass center of the binary. The four simplest coplanar configurations of CB-SMBHs and corresponding light curves are considered here when the companions pass through the periastron. Random accretion onto the CB-SMBHs makes the configuration more complicated. Tidal interaction leads to two kinds of quenching modes: (1) fast gains of angular momentum for prograde mini-disks (Case A) from the binary orbit; (2) precursor-flaring and quenching for a retrograde mini-disk (the secondary in Case B). The precursor-flaring is caused by the rapid loss of angular momentum of the tidal part so that it greatly enhances accretion of the rest part of the mini-disk. Here $\Delta L_{1,2} = \eta\,(\delta M_{\rm t}^{\rm p,s}/t_{\rm v}^{\rm p,s})\,c^2$ represent the increased luminosity (mainly in UV band) due to the elevated accretion for the primary and the secondary BHs, respectively. Adapted from Wang & Bon (2020).

configurations. The tidal timescale is

$$t_{\rm tid} = q^{1/2}\frac{R_{\rm g}}{c}\left(\frac{a}{R_{\rm g}}\right)^{3/2}\left(\frac{R_{\rm d}}{a}\right)^{-3/2} = 0.49\,M_8 q^{1/2}\left(\frac{a}{10^2R_{\rm g}}\right)^{3/2}\left(\frac{R_{\rm d}}{0.1a}\right)^{-3/2}\ {\rm yr}, \tag{26}$$

where $R_{\rm d}$ is the disk radius.

For prograde angular momentum configurations, the mini-disks beyond the tidal radius ($R_{\rm tid}$) will obtain angular momentum from the orbital and the $R_{\rm tid}$-disk becomes a decretion, and the inner part $\lesssim R_{\rm tid}$ will spiral into SMBHs on the viscosity timescale ($t_{\rm vis}$). After an interval of $t_{\rm tid}$, photoionizing source will be completely quenched, giving rise to type transition from type-1 to type-2. The decretion will accumulate with orbital motion, which radiates the observed optical continuum. During the transition, UV continuum undergoes the most violent variations, but the optical is relatively stable. For the retrograde mini-disks, the $R_{\rm tid}$-part will be squeezed into the central part and result in one giant flare on a timescale of $t_{\rm tid}$. It is then expected that the photoionizing source is stopped and a type transition happens.

When the binary black holes approach to the apastron, the peeling process prevails the tidal interaction and the $R_{\rm tid}$-disk will be accreted onto SMBHs again. Photoionizing sources of the two mini-disks rejuvenate and then the surrounding medium will be reionized appearing as type-1 AGNs. We should mention that the tidal action is only efficient in CB-SMBHs with high-e orbits. Many details along the entire orbits should be explored in future.

Nevertheless, this model demonstrates that tidal torques of companion black holes can completely change the fates of the mini-disks. It should be also mentioned that the continuum variations of the binary system could be aperiodic, but the type transitions should follow the orbits.

5 PROPERTIES OF NANO-HZ GRAVITATIONAL WAVES

The characteristic strain amplitude (sky- and polarization-averaged) of gravitational waves radiated by CB-SMBHs on circular orbits is (e.g., Thorne 1987)

$$\begin{aligned} h_s &= \left(\frac{128}{15}\right)^{1/2} \frac{(GM_c)^{5/3}}{c^4 d_c} (\pi f)^{2/3} \\ &= 1.9\times 10^{-15} \left(\frac{M_c}{10^8 M_\odot}\right)^{5/3} \left(\frac{d_c}{100\mathrm{Mpc}}\right)^{-1} \left(\frac{f}{10^{-9}\mathrm{Hz}}\right)^{2/3}, \end{aligned} \tag{27}$$

where d_c is the comoving distance to the CB-SMBH, f is the rest-frame GW frequency, which equals two times the orbital frequency (i.e., $f = 2/P_{\rm orb}$), and M_c is the chirping mass $M_c = (M_1 M_2)^{3/5} / (M_1 + M_2)^{1/5}$.

For a CB-SMBH with total mass of $10^8 M_\odot$ and an orbital period of 10 yr, the GW frequency is $f = 6 \times 10^{-9}$Hz, the orbital separation is $a \approx 0.01$ pc and the shrinking time scale is $t_{\rm GW}$ is about 10^6 yr. Such a low-frequency GW is detectable by PTAs through monitoring timing residuals in pulses from galactic millisecond pulsars (Hellings & Downs 1983). Due to the long shrinking time scale, the resulting PTA signals appear as continuous fluctuations in the timing residuals.

The superposition of GWs radiated from all population of CB-SMBHs distributed over various cosmic distances constitute the stochastic GW background. If only considering CB-SMBHs evolving purely due to GW emission, the characteristic strain of the GW background tends to follow a power law (e.g., Sesana et al. 2008),

$$h_c \propto A_0 \left(\frac{f}{1\,\mathrm{yr}^{-1}}\right)^{-2/3}, \tag{28}$$

where the amplitude depends on evolution models of CB-SMBHs, but is typically on the order of $A_0 = 10^{-15}$ (e.g., Sesana et al. 2008; Chen et al. 2020).

Currently, there are three PTA experiments in operation: the Parkes PTA (PPTA; Hobbs 2013), the European PTA (EPTA; Desvignes et al. 2016), and the North American Observatory for Gravitational Waves (NANOGrav; McLaughlin 2013). These three experiments together constitute an international collaboration, known as the International PTA (IPTA; Verbiest et al. 2016). The Square Kilometre Array (SKA) under construction will significantly improve timing precisions and enhance the sensitivity of nano-Hz GWs detection (e.g., Wang & Mohanty 2017; Feng et al. 2020). With accumulation of longer and more accurate pulsar timing data, PTA searches for the stochastic GW background are gradually approaching the sensitivities necessary to constrain the astrophysical limits on the population of CB-SMBHs (e.g., Shannon et al. 2015; Mingarelli et al. 2017; Arzoumanian et al. 2018). Meanwhile, efforts are also being made to search for continuous GW signals from individual CB-SMBHs (Zhu et al. 2014, 2015; Wang et al. 2015; Babak et al. 2016; Schutz & Ma 2016; Mingarelli et al. 2017; Feng et al. 2019), however, there is yet no a statistically significant detection.

6 ONGOING PROJECTS FOR CB-SMBHS

To our best knowledge, there are a few ongoing projects devoted to searching for CB-SMBH through electromagnetic observations. This is largely because of big challenges in designing practical and effective observational criterions for CB-SMBHs.

Monitoring AGNs with Hβ Asymmetry project (MAHA). This is a dedicated project through Wyoming Infrared Observatory (WIRO) 2.3m telescope (Du et al. 2018; Brotherton et al. 2020). The motivations of the project are to explore the geometry and kinematics of the gas responsible for asymmetry Hβ emission-line profiles, which can be explained by the existence of CB-SMBHs in AGNs. The project has continued uninterrupted for three years and is still ongoing. Several candidates (such as Mrk 6 and Ark 120) show potential features for CB-SMBHs.

Spectroscopic monitoring programs for AGNs with broad emission lines offsets. Eracleous et al. (2012) reported a selection of 88 AGN candidates for CB-SMBHs with significant offsets of the Hβ emission line by thousands of km s^{-1}. This sample was continuously spectroscopically monitored by a variety of ground-based facilities since 2009 (Runnoe et al. 2015, 2017). The latest publication by Runnoe et al. (2017) measured radial velocity variations of the broad Hβ lines and presented the radial velocity curves, from which they derived minimum limits on the total mass of CB-SMBHs based on the hypothesis that the velocity variations arise from the orbital motion. Using the similar approach, another group also performed searches for CB-SMBH candidates based on the multi-epoch SDSS spectroscopy of the broad Hβ line (Shen et al. 2013; Liu et al. 2014; Guo et al. 2019).

Modeling broad emission line profiles from CB-SMBHs. Nguyen & Bogdanović (2016) developed a semi-analytic model to describe spectral emission-line signatures of CB-SMBHs. This is helpful to the interpretation of spectroscopic searches for CB-SMBHs. The model was further improved by including the effect of radiation-driven accretion disk wind on properties of the emission line profiles (Nguyen et al. 2019) and then compared with observations of 88 CB-SMBH candidates that Eracleous et al. (2012) selected (Nguyen et al. 2020). Some orbital parameters for CB-SMBHs were thereby determined based on the CB-SMBH model.

7 OPEN QUESTIONS

Our current knowledge about CB-SMBHs is increasing, but still primitive. There are enormous open questions about CB-SMBHs, among which include (but not limited to):

– Are both black holes in CB-SMBHs in the status of accretion from their host galaxies? It is possible that either only one or both black holes are active. What kind of physical processes controls the activities of the two black holes?
– What are roles of orbital eccentricities of CB-SMBHs in long-term variations of continuum? In particular, tidal interaction between companion black holes and mini-disks could efficiently control the accretion status. Could these govern type transitions of AGNs show changing-look variations?
– The tidal torque of CB-SMBHs is an efficient way to transport angular momentum of interstellar medium (ISM) outward and govern accretion of infalling ISM gas. Are CB-SMBHs active in galaxies?
– Detailed physical processes related to CB-SMBH orbital evolution remain open, although the dynamic properties of the CBDs are expected to play an important role. This leads to significant uncertainties in evolution timescales of CB-SMBHs.
– What are the mass function and merger rates of CB-SMBHs? Due to the uncertainties in orbital evolution of CB-SMBHs, the mass function and merger rates of CB-SMBHs are largely unknown.
– Can the observed periods in variability be used to indicate the orbital periods of CB-SMBHs? Numerical simulations have found this is not the case for some ranges of mass ratios. Then a challenging issue is how to determine the orbital periods from periodic variations.
– What are the geometry and kinematics of BLRs in CB-SMBH systems? Reverberation mapping of normal AGNs generally reveals a thick disk-like geometry (Peterson 2014). The situation in CB-SMBH systems must be complicated and the BLR configurations are largely unknown.
– What are the differences in profiles of emission lines for CB-SMBHs at different orbital separations and eccentricities? A heuristic quest would be to build up a spectral sequence of CB-SMBHs along their separations. Exhaustive understandings on BLR geometry and kinematics in CB-SMBH systems are again required to address this issue.
– Last but not least, how to determine the full orbital parameters of CB-SBMBs? As mentioned above, PTA observations are unable to do so because of long-standing waveforms of nano-Hz GWs.

8 CONCLUSIONS

We reviewed several possible observational signatures of CB-SMBHs from theoretic expectations, numerical simulations, and observational considerations. Although there are not yet exclusive candidates of CB-SMBHs, searches for CB-SMBHs through various techniques and avenues are still compelling at the dawn of the multi-messager era. It is believed that the final identifications of true CB-SMBHs may have to resort to detection of GWs, but systematic searches and studies of CB-SMBH candidates based on electromagnetic observations at any rate are necessary and important, considering the yet challenges in PTA detections of nano-Hz GWs radiated by CB-SMBHs. In particular, GW waveforms at nona-Hz frequency evolves fairly too slowly to detect the chirping phases in a reasonable human timescale, making PTA detections impossible to determine the full orbital parameters of individual CB-SMBHs. Other independent methods through electromagnetic observations have to be involved, such as the reverberation mapping technique and spectroastrometry technique with high spatial resolution (realized at the GRAVITY/VLTI). Combined with a growing sophistication of numerical simulations of CB-SMBHs and improved theoretical predictions for electromagnetic and GW signatures, there are great promises for detecting CB-SMBHs in the next decades. This will then open up a new chapter in studies of cosmic growth and evolution of SMBHs.

Acknowledgements We acknowledge financial support from the National Natural Science Foundation of China (11833008 and 11991054), from the National Key R&D Program of China (2016YFA0400701), from the Key Research Program of Frontier Sciences of the Chinese Academy of Sciences (CAS; QYZDJ-SSW-SLH007), and from the CAS Key Research Program (KJZD-EW-M06).

References

Antonucci, R. 1993, ARA&A, 31, 473
Antonucci, R. R. J., & Miller, J. S. 1985, ApJ, 297, 621
Artymowicz, P., & Lubow, S. H. 1994, ApJ, 421, 651
Artymowicz, P., & Lubow, S. H. 1996, ApJL, 467, L77
Arzoumanian, Z., Baker, P. T., Brazier, A., et al. 2018, ApJ, 859, 47
Babak, S., Petiteau, A., Sesana, A., et al. 2016, MNRAS, 455, 1665

Bankert, J., Krolik, J. H., & Shi, J. 2015, ApJ, 801, 114
Beckers, J. M. 1982, Optica Acta, 29, 361
Begelman, M. C., Blandford, R. D., & Rees, M. J. 1980, Nature, 287, 307
Bellm, E. C., Kulkarni, S. R., Graham, M. J., et al. 2019, PASP, 131, 018002
Bentz, M. C., Denney, K. D., Grier, C. J., et al. 2013, ApJ, 767, 149
Berczik, P., Merritt, D., Spurzem, R., & Bischof, H.-P. 2006, ApJL, 642, L21
Bon, E., Jovanović, P., Marziani, P., et al. 2012, ApJ, 759, 118
Bon, E., Zucker, S., Netzer, H., et al. 2016, ApJS, 225, 29
Bowen, D. B., Mewes, V., Noble, S. C., et al. 2019, ApJ, 879, 76
Brotherton, M. *et al.*. 2020, ApJ, Submitted
Cabell, R. H., Lester, H. C., & Silcox, R. J. 1992, in Proposed for Presentation at the 1992 International Congress on Noise Control Engineering (INTER-NOISE), 92, 20
Charisi, M., Bartos, I., Haiman, Z., et al. 2016, MNRAS, 463, 2145
Chen, Y., Yu, Q., & Lu, Y. 2020, ApJ, 897, 86
Colpi, M. 2014, Space Sci. Rev., 183, 189
Combes, F., García-Burillo, S., Audibert, A., et al. 2019, A&A, 623, A79
Comerford, J. M., Schluns, K., Greene, J. E., & Cool, R. J. 2013, ApJ, 777, 64
Cuadra, J., Armitage, P. J., Alexander, R. D., & Begelman, M. C. 2009, MNRAS, 393, 1423
De Rosa, A., Vignali, C., Bogdanović, T., et al. 2019, New Astron. Rev., 86, 101525
Desvignes, G., Caballero, R. N., Lentati, L., et al. 2016, MNRAS, 458, 3341
Doan, A., Eracleous, M., Runnoe, J. C., et al. 2020, MNRAS, 491, 1104
D'Orazio, D. J., Haiman, Z., & Schiminovich, D. 2015, Nature, 525, 351
Dotti, M., Sesana, A., & Decarli, R. 2012, Advances in Astronomy, 2012, 940568
Du, P., & Wang, J.-M. 2019, ApJ, 886, 42
Du, P., Brotherton, M. S., Wang, K., et al. 2018, ApJ, 869, 142
Dyda, S., Lovelace, R. V. E., Ustyugova, G. V., et al. 2015, MNRAS, 446, 613
Ebisuzaki, T., Makino, J., & Okumura, S. K. 1991, Nature, 354, 212
Eggleton, P. P. 1983, ApJ, 268, 368
eLISA Consortium, Amaro Seoane, P., Aoudia, S., et al. 2013, arXiv e-prints, arXiv:1305.5720
Eracleous, M., Boroson, T. A., Halpern, J. P., & Liu, J. 2012, ApJS, 201, 23
Escala, A., Larson, R. B., Coppi, P. S., & Mardones, D. 2005, ApJ, 630, 152
Farris, B. D., Duffell, P., MacFadyen, A. I., & Haiman, Z. 2014, ApJ, 783, 134
Farris, B. D., Duffell, P., MacFadyen, A. I., & Haiman, Z. 2015, MNRAS, 446, L36
Feng, Y., Li, D., Li, Y.-R., & Wang, J.-M. 2019, RAA (Research in Astronomy and Astrophysics), 19, 178
Feng, Y., Li, D., Zheng, Z., & Tsai, C.-W. 2020, Phys. Rev. D, 102, 023014
Flaugher, B., & Bebek, C. 2014, in SPIE Conference Series, 9147, Ground-based and Airborne Instrumentation for Astronomy V, 91470S
Fu, H., Myers, A. D., Djorgovski, S. G., et al. 2015, ApJ, 799, 72
Ge, J.-Q., Hu, C., Wang, J.-M., Bai, J.-M., & Zhang, S. 2012, ApJS, 201, 31
Goicovic, F. G., Maureira-Fredes, C., Sesana, A., Amaro-Seoane, P., & Cuadra, J. 2018, MNRAS, 479, 3438
Goicovic, F. G., Sesana, A., Cuadra, J., & Stasyszyn, F. 2017, MNRAS, 472, 514
Graham, M. J., Djorgovski, S. G., Stern, D., et al. 2015a, Nature, 518, 74
Graham, M. J., Djorgovski, S. G., Stern, D., et al. 2015b, MNRAS, 453, 1562
Greenhill, L. J., & Gwinn, C. R. 1997, Ap&SS, 248, 261
Gültekin, K., & Miller, J. M. 2012, ApJ, 761, 90
Guo, H., Liu, X., Shen, Y., et al. 2019, MNRAS, 482, 3288
Guo, H., Liu, X., Tayyaba, Z., & Liao, W.-T. 2020, MNRAS, 492, 2910
Hayasaki, K., Mineshige, S., & Ho, L. C. 2008, ApJ, 682, 1134
Hellings, R. W., & Downs, G. S. 1983, ApJL, 265, L39
Hobbs, G. 2013, Classical and Quantum Gravity, 30, 224007
Hutsemékers, D., Agís González, B., Marin, F., et al. 2019, A&A, 625, A54
Imanishi, M., Nakanishi, K., Izumi, T., & Wada, K. 2018, ApJL, 853, L25
Impellizzeri, C. M. V., Gallimore, J. F., Baum, S. A., et al. 2019, ApJL, 884, L28
Ivezic, Z., Axelrod, T., Brandt, W. N., et al. 2008, Serbian Astronomical Journal, 176, 1
Kharb, P., Lal, D. V., & Merritt, D. 2017, Nature Astronomy, 1, 727
Komossa, S. 2006, Mem. Soc. Astron. Italiana, 77, 733
Kovačević, A. B., Wang, J.-M., & Popović, L. Č. 2020, A&A, 635, A1
Leighly, K. M., Terndrup, D. M., Gallagher, S. C., & Lucy, A. B. 2016, ApJ, 829, 4
Li, Y.-R., Wang, J.-M., Ho, L. C., et al. 2016, ApJ, 822, 4
Li, Y.-R., Wang, J.-M., Zhang, Z.-X., et al. 2019, ApJS, 241, 33
Lin, D. N. C., & Papaloizou, J. 1986, ApJ, 307, 395
Liu, T., Gezari, S., Ayers, M., et al. 2019, ApJ, 884, 36
Liu, X., Lazio, T. J. W., Shen, Y., & Strauss, M. A. 2018, ApJ, 854, 169
Liu, X., Shen, Y., Bian, F., Loeb, A., & Tremaine, S. 2014, ApJ, 789, 140
Lodato, G., Nayakshin, S., King, A. R., & Pringle, J. E. 2009, MNRAS, 398, 1392
Lyke, B. W., Higley, A. N., McLane, J. N., et al. 2020, ApJS, 250, 8
MacFadyen, A. I., & Milosavljević, M. 2008, ApJ, 672, 83
MacLeod, C. L., Ross, N. P., Lawrence, A., et al. 2016, MNRAS, 457, 389

MacLeod, C. L., Green, P. J., Anderson, S. F., et al. 2019, ApJ, 874, 8
Marin, F., Hutsemékers, D., & Agís González, B. 2019, in SF2A-2019: Proceedings of the Annual meeting of the French Society of Astronomy and Astrophysics, eds. P. Di Matteo, O. Creevey, A. Crida, G. Kordopatis, J. Malzac, J. B. Marquette, M. N'Diaye, & O. Venot, Di
Mayer, L., Kazantzidis, S., Madau, P., et al. 2007, Science, 316, 1874
McLaughlin, M. A. 2013, Classical and Quantum Gravity, 30, 224008
Merritt, D. 2006, ApJ, 648, 976
Merritt, D., & Ekers, R. D. 2002, Science, 297, 1310
Milosavljević, M., & Merritt, D. 2001, ApJ, 563, 34
Milosavljević, M., Merritt, D., Rest, A., & van den Bosch, F. C. 2002, MNRAS, 331, L51
Mingarelli, C. M. F., Lazio, T. J. W., Sesana, A., et al. 2017, Nature Astronomy, 1, 886
Müller Sánchez, F., Davies, R. I., Genzel, R., et al. 2009, ApJ, 691, 749
Netzer, H. 2015, ARA&A, 53, 365
Nguyen, K., & Bogdanović, T. 2016, ApJ, 828, 68
Nguyen, K., Bogdanović, T., Runnoe, J. C., et al. 2019, ApJ, 870, 16
Nguyen, K., Bogdanović, T., Runnoe, J. C., et al. 2020, ApJ, 894, 105
Nixon, C. J., Cossins, P. J., King, A. R., & Pringle, J. E. 2011, MNRAS, 412, 1591
Nixon, C., & Lubow, S. H. 2015, MNRAS, 448, 3472
Noble, S. C., Mundim, B. C., Nakano, H., et al. 2012, ApJ, 755, 51
Osterbrock, D. E., & Mathews, W. G. 1986, ARA&A, 24, 171
Papaloizou, J., & Pringle, J. E. 1977, MNRAS, 181, 441
Pérol, P. 1998, in ESA Special Publication, 416, in Proceedings of the Fifth ESPC, ed. R. A. Harris, 39
Peters, P. C. 1964, Physical Review, 136, 1224
Peterson, B. M. 1993, PASP, 105, 247
Peterson, B. M. 2014, Space Sci. Rev., 183, 253
Popović, L. Č. 2012, New Astron. Rev., 56, 74
Popovic, L. C., Mediavilla, E. G., & Pavlovic, R. 2000, Serbian Astronomical Journal, 162, 1
Quach, D., Dyda, S., & Lovelace, R. V. E. 2015, MNRAS, 446, 622
Rees, M. J. 1984, ARA&A, 22, 471
Roedig, C., & Sesana, A. 2014, MNRAS, 439, 3476
Roedig, C., Sesana, A., Dotti, M., et al. 2012, A&A, 545, A127
Ross, N. P., Ford, K. E. S., Graham, M., et al. 2018, MNRAS, 480, 4468
Runnoe, J. C., Eracleous, M., Mathes, G., et al. 2015, ApJS, 221, 7
Runnoe, J. C., Eracleous, M., Pennell, A., et al. 2017, MNRAS, 468, 1683
Savić, D., Marin, F., & Popović, L. Č. 2019, A&A, 623, A56
Schutz, K., & Ma, C.-P. 2016, MNRAS, 459, 1737
Sesana, A., Roedig, C., Reynolds, M. T., & Dotti, M. 2012, MNRAS, 420, 860
Sesana, A., Vecchio, A., & Colacino, C. N. 2008, MNRAS, 390, 192
Shannon, R. M., Ravi, V., Lentati, L. T., et al. 2015, Science, 349, 1522
Shen, Y., Liu, X., Loeb, A., & Tremaine, S. 2013, ApJ, 775, 49
Shen, Y., & Loeb, A. 2010, ApJ, 725, 249
Shi, J.-M., & Krolik, J. H. 2016, ApJ, 832, 22
Shi, J.-M., Krolik, J. H., Lubow, S. H., & Hawley, J. F. 2012, ApJ, 749, 118
Smith, J. E., Robinson, A., Young, S., Axon, D. J., & Corbett, E. A. 2005, MNRAS, 359, 846
Songsheng, Y.-Y., Wang, J.-M., & Li, Y.-R. 2019, ApJ, 883, 184
Songsheng, Y.-Y., Xiao, M., Wang, J.-M., & Ho, L. C. 2020, ApJS, 247, 3
Tanaka, T. L., & Haiman, Z. 2013, Classical and Quantum Gravity, 30, 224012
Temi, P., Amblard, A., Gitti, M., et al. 2018, ApJ, 858, 17
Thorne, K. S. 1987, Gravitational Radiation, ed. S. H. W. Israel, Three Hundred Years of Gravitation (Cambridge: Cambridge Univ. Press), 330
Tremblay, G. R., Oonk, J. B. R., Combes, F., et al. 2016, Nature, 534, 218
Valtonen, M. J., Lehto, H. J., Nilsson, K., et al. 2008, Nature, 452, 851
Vaughan, S., Uttley, P., Markowitz, A. G., et al. 2016, MNRAS, 461, 3145
Veilleux, S., Meléndez, M., Tripp, T. M., Hamann, F., & Rupke, D. S. N. 2016, ApJ, 825, 42
Verbiest, J. P. W., Lentati, L., Hobbs, G., et al. 2016, MNRAS, 458, 1267
Volonteri, M., Madau, P., & Haardt, F. 2003, ApJ, 593, 661
Wang, J. B., Hobbs, G., Coles, W., et al. 2015, MNRAS, 446, 1657
Wang, J.-M., Chen, Y.-M., Hu, C., et al. 2009, ApJL, 705, L76
Wang, J.-M., Songsheng, Y.-Y., Li, Y.-R., Du, P., & Yu, Z. 2020, MNRAS, 497, 1020
Wang, J.-M., & Bon, E. 2020, A&A Letters, in press
Wang, J.-M., Songsheng, Y.-Y., Li, Y.-R., & Yu, Z. 2018, ApJ, 862, 171
Wang, J. X., & Ip, W.-H. 2020, RAA (Research in Astronomy and Astrophysics), 20, 157
Wang, M. X., Luo, A. L., Song, Y. H., et al. 2019, MNRAS, 482, 1889
Wang, X. W., & Yuan, Y. F. 2012, MNRAS, 427, L1
Wang, Y., & Mohanty, S. D. 2017, Phys. Rev. Lett., 118, 151104
Yan, C.-S., Lu, Y., Dai, X., & Yu, Q. 2015, ApJ, 809, 117
Yan, C.-S., Lu, Y., Yu, Q., Mao, S., & Wambsganss, J. 2014, ApJ, 784, 100
Yu, Q. 2002, MNRAS, 331, 935
Zhang, P.-f., Yan, D.-h., Zhou, J.-n., Wang, J.-c., & Zhang, L. 2020, ApJ, 891, 163
Zheng, Z.-Y., Butler, N. R., Shen, Y., et al. 2016, ApJ, 827, 56
Zhu, X. J., Hobbs, G., Wen, L., et al. 2014, MNRAS, 444, 3709
Zhu, X. J., Wen, L., Hobbs, G., et al. 2015, MNRAS, 449, 1650